

This is a repository copy of *Extended-magnetohydrodynamics in under-dense plasmas*.

White Rose Research Online URL for this paper:

<https://eprints.whiterose.ac.uk/160567/>

Version: Accepted Version

---

**Article:**

Walsh, C. A., Chittenden, J. P., Hill, D. W. [orcid.org/0000-0002-6218-7048](https://orcid.org/0000-0002-6218-7048) et al. (1 more author) (2020) *Extended-magnetohydrodynamics in under-dense plasmas*. *Physics of Plasmas*. 022103. ISSN 1089-7674

<https://doi.org/10.1063/1.5124144>

---

**Reuse**

This article is distributed under the terms of the Creative Commons Attribution (CC BY) licence. This licence allows you to distribute, remix, tweak, and build upon the work, even commercially, as long as you credit the authors for the original work. More information and the full terms of the licence here:

<https://creativecommons.org/licenses/>

**Takedown**

If you consider content in White Rose Research Online to be in breach of UK law, please notify us by emailing [eprints@whiterose.ac.uk](mailto:eprints@whiterose.ac.uk) including the URL of the record and the reason for the withdrawal request.

# Extended-Magnetohydrodynamics in Under-dense Plasmas

C. A. Walsh,<sup>1, a)</sup> J. P. Chittenden,<sup>1</sup> D. W. Hill,<sup>2</sup> and C. Ridgers<sup>2</sup>

<sup>1)</sup>*Blackett Laboratory, Imperial College, London, United Kingdom, SW7 2AZ*

<sup>2)</sup>*York Plasma Institute, Genesis 1&2, York Science Park, University of York, Church Lane, Heslington, United Kingdom, YO10 5DQ*

(Dated: 18 December 2019)

Extended-magnetohydrodynamics transports magnetic flux and electron energy in high-energy-density experiments, but individual transport effects remain unobserved experimentally. Two factors are responsible in defining the transport: electron temperature and electron current. Each electron energy transport term has a direct analogue in magnetic flux transport. To measure the thermally-driven transport of magnetic flux and electron energy, a simple experimental configuration is explored computationally using a laser-heated pre-magnetised under-dense plasma. Changes to the laser heating profile precipitate clear diagnostic signatures from the Nernst, cross-gradient-Nernst, anisotropic conduction and Righi-Leduc heat-flow. With a wide operating parameter range, this configuration can be used in both small and large scale facilities to benchmark MHD and kinetic transport in collisional/semi-collisional, local/non-local and magnetised/unmagnetised regimes.

## I. INTRODUCTION

Extended-Magnetohydrodynamics (extended-MHD) is a theoretical framework used to evaluate the transport of energy and magnetic flux in a plasma. The electrons typically move at a higher speed than the ions, dominating the transport. Additional terms introduced by extended-MHD above resistive-MHD include temperature-gradient-driven transport (such as the Nernst term moving magnetic fields down electron temperature gradients) and electric-current-driven transport (such as the Hall term moving magnetic fields with the flow of charge). For each magnetic transport term there is a corresponding transport of electron energy; for example, the analogue of Nernst in energy transport is thermal conduction, which moves thermal energy down temperature gradients.

Extended-MHD terms are anticipated to be important in a wide range of high energy-density physics (HEDP) experiments. The Nernst effect limits the performance of magnetised liner inertial fusion (MagLIF) implosions by demagnetising the pre-heated fuel<sup>1</sup>. The design of laser-driven pre-magnetised inertial confinement fusion (ICF) targets<sup>2,3</sup>, also requires the consideration of these additional effects<sup>4</sup>. Even initially unmagnetised ICF configurations can be affected by extended-MHD phenomena, with self-generated fields growing through the Biermann battery process. Simulation studies have found the Nernst (magnetic fields moving down temperature gradients) and Righi-Leduc (heat-flow deflected by the magnetic field) terms to change plasma properties in hohlraums (increasing the temperature of the hohlraum gas fill<sup>5</sup>), direct-drive ablation fronts (changing the perturbation growth<sup>6</sup>) and at the compressed fusion-fuel edge (modifying the cooling process<sup>7</sup>). In addition to

ICF, extended-MHD affects laboratory astrophysics experiments, such as the measurement of magnetic fields generated around laser-foil interactions<sup>8,9</sup> and are anticipated to also affect 2-spot magnetic reconnection<sup>10</sup>.

While the impact of extended-MHD is widespread in laboratory HEDP, many of the effects are yet to be measured directly. Without experimental verification of the extended-MHD model, uncertainties remain in the design and analysis of ICF and laboratory astrophysics studies. A notable exception is the Biermann battery term, with time-dependent magnetic field generation measured around a laser-foil interaction<sup>8</sup>, in addition to systems exhibiting Rayleigh-Taylor instability growth<sup>11</sup>. In both of these examples the Nernst term significantly alters the magnetic field distribution, but the experimental complexity prohibited direct inference of a Nernst velocity to compare with simulations. Other key properties of Nernst advection, such as suppression of the effect at large magnetisations, also remain unverified.

This paper uses simulations to investigate experimental configurations where thermally-driven extended-MHD terms (Nernst, cross-gradient-Nernst, anisotropic thermal conduction and Righi-Leduc heat-flow) could be measured unambiguously for the first time. An under-dense laser-driven magnetised plasma is used, allowing for the thermally-driven transport to dominate over the hydrodynamic motion. Clear diagnostic signatures are sought for each term through simple modifications to the laser profile. A similar set-up has been used before without the diagnosis of magnetic field distribution to measure non-local heat-flow suppression<sup>12</sup>, with subsequent kinetic simulations suggesting that both Nernst and non-locality are important<sup>13</sup>. Non-local transport is outside the scope of this paper, with the plasma treated using an MHD framework. Changes to the experimental set-up can then be used to explore different regimes, such as the transition from extended-MHD to kinetic transport for each of the terms.

This paper is organised as follows. The appendix rewrites the traditional Braginskii extended-MHD equa-

---

<sup>a)</sup>Electronic mail: c.walsh14@imperial.ac.uk

tions into a form that is both physically intuitive and simple to implement into an MHD code. This is then summarised in section II, with each of the relevant transport terms clearly formed. Section III A then outlines an experiment to measure Nernst cavitation of a magnetic field in an under-dense plasma, showing simulation results as well as synthetic diagnostics. This set-up provides a baseline configuration, which is modified to explore other extended-MHD terms. By changing the laser focus, the cross-gradient-Nernst twists the magnetic field, as shown in section III B. Anisotropic thermal conduction is then demonstrated in section III C by using an applied magnetic field perpendicular to the beam rather than parallel. Finally, section III D takes the Nernst experiment but uses a non-circular laser spot to elucidate the Righi-Leduc heat-flow in the form of a rotation of the thermal profile.

## II. EXTENDED-MAGNETOHYDRODYNAMICS

Magnetic transport in an extended-MHD plasma is explored in the appendix, beginning with Braginskii's formulation of Ohm's Law<sup>14</sup>. The following equation is derived for the change of magnetic field strength:

$$\frac{\partial \underline{B}}{\partial t} = -\nabla \times \frac{\alpha_{\parallel}}{\mu_0 e^2 n_e^2} \nabla \times \underline{B} + \nabla \times (\underline{v}_B \times \underline{B}) + \nabla \times \frac{\nabla P_e}{en_e} \quad (1)$$

There are only 3 terms: one for magnetic field diffusion, one for advection of the magnetic field at velocity  $\underline{v}_B$  and the Biermann Battery term as the only source of magnetic flux. The magnetic field advection velocity  $\underline{v}_B$  is given by:

$$\underline{v}_B = \underline{v} - \gamma_{\perp} \nabla T_e - \gamma_{\wedge} (\hat{\underline{b}} \times \nabla T_e) - \frac{\underline{j}}{en_e} (1 + \delta_{\perp}^c) + \frac{\delta_{\wedge}^c}{en_e} (\underline{j} \times \hat{\underline{b}}) \quad (2)$$

i.e. the advection is based on the bulk plasma velocity, as well as the electron temperature gradient and electric current. The  $\gamma_{\perp}$  term is called the Nernst term, which moves magnetic field down temperature gradients. The  $\gamma_{\wedge}$  term is then the cross-gradient-Nernst, moving the field perpendicular to both the temperature gradient and the magnetic field. Both  $\gamma_{\perp}$  and  $\gamma_{\wedge}$  simply decrease with magnetisation  $\omega_e \tau_e$  (see figure 8).

The electron temperature gradient and electric current also cause transport of electron energy. To make the physical connection between magnetic and energy transport clear, the magnetic field advection velocity due to electron temperature gradients are shown alongside the heat-flow due to electron temperature gradients:

$$\underline{v}_N = -\gamma_{\perp} \nabla_{\perp} T_e - \gamma_{\wedge} \hat{\underline{b}} \times \nabla T_e \quad (3)$$

$$\underline{q}_{\kappa} = -\kappa_{\parallel} \nabla_{\parallel} T_e - \kappa_{\perp} \nabla_{\perp} T_e - \kappa_{\wedge} \hat{\underline{b}} \times \nabla T_e \quad (4)$$

where there is no field advection parallel to the field lines, as this does not change the magnetic flux. The

thermal conduction perpendicular to magnetic field lines  $\kappa_{\perp}$  is seen here to be associated with the Nernst  $\gamma_{\perp}$  term. Comparably, the Righi-Leduc heat-flow  $\kappa_{\wedge}$  acts to move electron energy in the same direction as the cross-gradient-Nernst  $\gamma_{\wedge}$  moves magnetic flux.

In a similar way, the electric-current-driven magnetic field advection velocity and energy advection velocity can be written:

$$\underline{v}_{jB} = -(1 + \delta_{\perp}^c) \frac{\underline{j}_{\perp}}{en_e} + \delta_{\wedge}^c \left( \frac{\underline{j}}{en_e} \times \hat{\underline{b}} \right) \quad (5)$$

$$\underline{v}_{jU_e} = -(1 + \beta_{\parallel}^c) \frac{\underline{j}_{\parallel}}{en_e} - (1 + \beta_{\perp}^c) \frac{\underline{j}_{\perp}}{en_e} + \beta_{\wedge}^c \left( \frac{\underline{j}}{en_e} \times \hat{\underline{b}} \right) \quad (6)$$

In these simplified forms, a non-dimensional number can be used to assess if temperature gradients or electric currents dominate the transport. Assuming that the magnetic field varies over the same length-scale as the temperature:

$$\Xi = \frac{|\underline{v}_{N\perp}|}{|\underline{v}_{jB\perp}|} = \frac{\gamma_{\perp}^c \tau_e T_e en_e \mu_0}{|\underline{B}| m_e} \sim \frac{\gamma_{\perp}^c T_e^{\frac{5}{2}}}{|\underline{B}|} \quad (7)$$

Where the  $\delta_{\perp}^c$  factor is dropped as it is only a small correction to the collisionless current-driven magnitude (Hall). In a regime where thermally-driven terms dominate ( $\Xi \gg 1$ ) both the thermally-driven magnetic transport and thermally-driven electron energy transport will be significant. In a regime where current-driven terms dominate ( $\Xi \ll 1$ ) both current-driven magnetic transport and current-driven electron energy transport will be significant.

The appendix studies more closely the different magnetic field and electron energy transport terms, comparing the coefficients and outlining simply how to include these terms in an extended-MHD code.

## III. THERMALLY-DRIVEN TRANSPORT EXPERIMENTS

This section outlines a set of simple experiments to verify the thermally-driven magnetic and electron energy transport in equation 3 and 4. Section III A outlines the baseline configuration for measuring the Nernst velocity, which is then modified in the subsequent sections in order to allow the other terms to be measurable.

The parameters used in this publication are:

- Gas density  $\rho_0 = 0.065 \text{ kg/m}^3$
- Gas composition = deuterium
- Laser energy =  $50 \text{ J}$  with wavelength of  $1.055 \mu\text{m}$

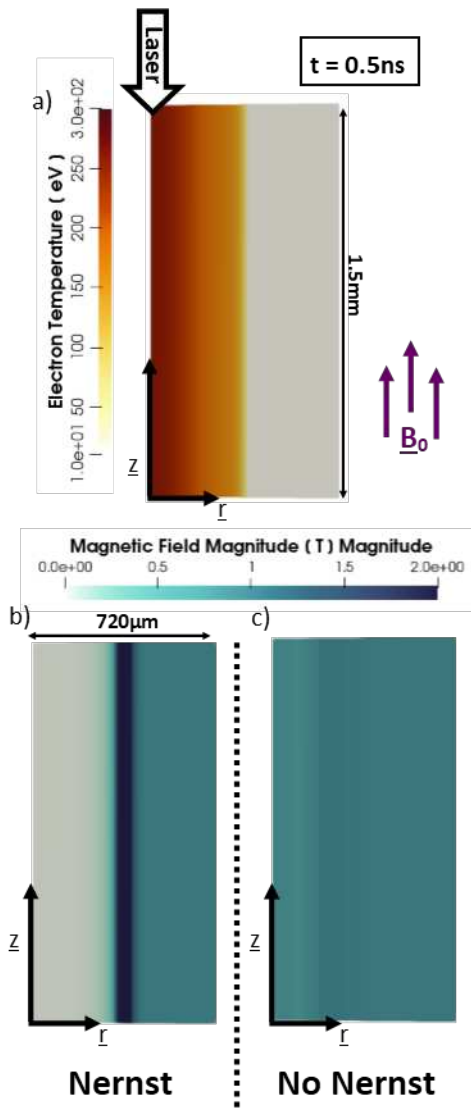


FIG. 1. 2-D cylindrical simulations of the Nernst configuration at 0.5ns with a 1T applied field. a) electron temperature with Nernst included. b) magnetic field magnitude with the Nernst effect included. c) magnetic field magnitude without the Nernst effect included. The magnetic field cavitation is strongly driven by Nernst advection.

- Laser spot spatial profile = Gaussian with standard deviation of  $75\mu m$
- Laser time profile =  $0.5ns$  with a  $0.1ns$  linear rise
- Applied magnetic field magnitude  $B_0 = 0 - 10T$

These parameters are realisable in a relatively small-scale facility and give a reasonable signal for the extended-MHD terms considered here. There is ample room for moving into different regions of parameter space, thereby modifying the transport rates and providing additional tests against theory. Lower laser energies ( $< 1J$ ) are also expected to give appreciable signals.

The ionised electron density relative to the laser critical density is small  $n_e/n_{cr} = 0.0190$ , i.e. the gas is under-dense. The low density allows for the laser to pass through without depositing significant amounts of energy; laser energy coupling into the simulation domains shown here are between 1-5% over 1.5mm. Increasing the coupling (e.g. using a higher density gas) would allow for even lower laser energies, although this would decrease temperature uniformity along the laser axis and increase laser refraction effects.

For the parameters chosen, thermally-driven transport terms dominate, i.e.  $\Xi$  is large (from equation 7).

The extended-MHD code Gorgon<sup>7,15</sup> is used to simulate the configurations, with distinct diagnostic signatures anticipated for each of the effects. Gorgon is a 2-temperature Eulerian code with laser ray tracing and absorption by inverse Bremsstrahlung. The magnetic transport is treated as in equation 1, using operator splitting between the advection, diffusion and generation components. The electron heat-flow is fully anisotropic, as in equation 34, using a centred-symmetric algorithm<sup>16</sup>. For the configurations in this paper the spatial resolution is  $0.5\mu m$ .

Synthetic proton deflectometry is used here to diagnose magnetic field transport. A  $D^3He$  exploding pusher is taken as the source, producing mono-energetic protons at 14.7MeV<sup>17</sup>. Target-normal sheath acceleration (TNSA)<sup>18,19</sup> could also be used. The source offset is taken as 6.3mm with the image plate 120mm from the interaction region. The source is assumed to be infinitely small, thereby reducing blurring. Electric field contributions to the proton images are estimated to be small.

### A. Nernst

A uniform under-dense ( $n_e \ll n_{crit}$ ) plasma is used, with a uniform magnetic field applied along the direction of laser propagation.

Simulations are conducted in 2-D cylindrical geometry ( $r - z$ ). The laser and magnetic field are applied in the direction  $-z$ , which assumes the laser is uniform azimuthally (in  $\theta$ ).

The laser-heated plasma becomes more transparent to the laser as the temperature increases, resulting in relatively uniform heating along the laser axis. Figure 1 shows the electron temperature at 0.5ns using the baseline parameters described in section III and a 1T applied field.

Thermal conduction transports heat radially away from the laser into the cold gas. Nernst advection, which is analogous to magnetic field moving with the heat-flow, reduces the field intensity in the laser-heated region. The demagnetising effect of the Nernst term is compounded by the increase in Nernst velocity as magnetisation decreases, further enhancing the demagnetisation rate. The magnetic field intensity is plotted in figure 1. In the regime shown, near complete magnetic cavitation is ob-

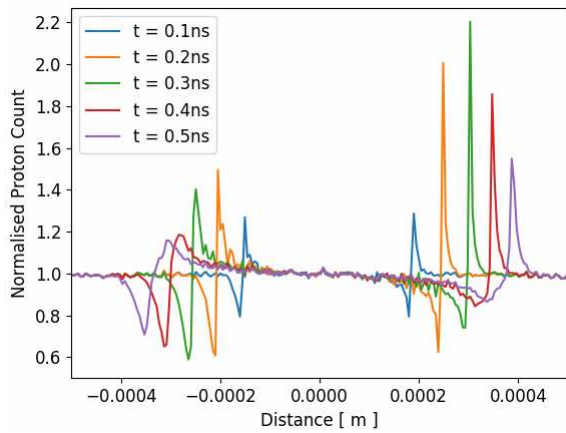


FIG. 2. Time-dependent synthetic proton radiographs for the Nernst configuration with an initial magnetic field of 1T. The Nernst velocity could be measured for the first time using this technique. While the distance between the edges ( $\lambda$ ) gives the cavitation rate, there is also information within the individual edges. The background magnetic field deflects protons towards the right of this image. The distance has been re-scaled to the interaction region using the set-up magnification.

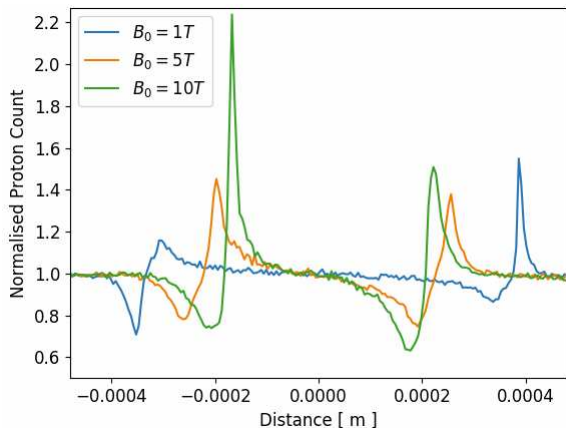


FIG. 3. Synthetic proton radiographs for the Nernst configuration at 0.5ns for 1T, 5T and 10T applied magnetic fields. Nernst suppression for higher magnetisations could be measured for the first time using this technique. The background magnetic field deflects protons towards the right of this image. The distance has been re-scaled to the interaction region using the set-up magnification and each field strength has been re-centred for comparison purposes.

served. The thermal wave corresponds with a discrete step in magnetic field intensity. The field is compressed at the edge of the heat front and can resistively diffuse away depending on whether or not the plasma is initialised as cold in the simulations.

Magnetic fields also move with the bulk plasma motion (so-called frozen-in-flow). As the laser-heated region expands, the magnetic field strength decreases. A definitive measure of the Nernst effect is simpler if the Nernst velocity is much larger than the hydrodynamic expansion.

Figure 1 quantifies the relative impact of Nernst advection by also showing the magnetic field profile for a simulation without the Nernst term included. In this case, the Nernst term is clearly dominating over the hydrodynamic motion. For the case without Nernst, the magnetic field strength  $|\underline{B}| = \rho B_0 / \rho_0$ . Significant hydrodynamic motion does not strictly prohibit a measurement of the Nernst velocity; a simultaneous density measurement can be used to infer that the magnetic field is not frozen into the flow.

Experimentally, the key measurements to constrain the Nernst effect involve measuring the field cavitation rate and the decrease in cavitation with a larger applied field. The field cavitation is diagnosed synthetically using proton radiography with protons traversing the system perpendicular to the initial magnetic field axis. Figure 2 shows proton deflectometry evolution with time. An average over the length of  $z$  in figure 1 is used. While all protons are deflected by the background magnetic field, the protons passing through the cavity are deflected less. This creates distinct regions with higher and lower proton counts at the cavity edge. The separation distance of these regions,  $\lambda$ , indicates the cavitation region size, which increases with time. The Nernst velocity can then be inferred through measurement of  $\partial\lambda/\partial t$ . Structure in the proton image at each of the cavitation edges could then provide more information on the compressed field profile, although this measurement requires higher resolution. Further information can be extracted from the proton radiographs by using a grid and assuming small proton deflections<sup>20</sup>; cylindrical symmetry allows the path-integrated magnetic field to be calculated.

Combining proton radiographs with Thomson scattering and interferometry diagnostics can be used to constrain the electron temperature and density; experimental and theoretical Nernst advection rates can then be compared without the need to estimate plasma properties from simulations.

The separation distance on the proton radiograph,  $\lambda$ , can be related to the cavitation radius  $r_c$  by assuming a uniform completely cavitating cylinder (i.e. fully demagnetised from initial magnetic field strength  $B_0$  to 0T) probed by protons of initial velocity  $v_p$  undergoing only small deflections, with the distance from the cylinder to image plate as  $D$ :

$$\lambda = \frac{eB_0 2r_c D}{m_p v_p} \quad (8)$$

For an increased background magnetic field, the above relation predicts that the offset distance increases for a given cavitation radius. Synthetic proton radiographs at 0.5ns for varying magnetic field strengths are shown in figure 3. Instead of  $\lambda$  increasing, the offset distance decreases due to Nernst suppression by magnetisation. The proton deposition structure at each cavity edge is more apparent for larger applied magnetic fields, allowing for a finer resolution of the magnetic field profile. In par-

ticular, an experimental measurement of the non-local 'pre-Nernst' may be possible<sup>21</sup> in these regions. If the gas outside of the heat front remains cold and unionised, then the magnetic field can diffuse away, removing the small-scale structure within the cavity edges in the proton radiographs.

An assessment of whether Nernst or hydrodynamic advection demagnetises the plasma can be explored more generally using a simple comparison of characteristic velocities. The Nernst velocity (from equation 20) is  $-\gamma_{\perp}^c \tau_e \nabla T_e / m_e$ . Unlike the near-instantaneous Nernst velocity, the bulk plasma has inertia and takes time to be accelerated to a significant velocity by the pressure imbalance. From simple hydrodynamics this velocity can be taken as  $\Delta t \nabla P / \rho$ . By using the fact that the density is initially uniform (overestimating the impact of hydrodynamics) the relative magnitude of hydrodynamics to Nernst advection can be estimated:

$$\frac{|\underline{v}_{Hydro}|}{|\underline{v}_{N\perp}|} = \frac{\Delta t Z m_e}{\tau_e m_i} \frac{1}{\gamma_{\perp}^c} \quad (9)$$

$Z m_e / m_i$  varies little between the choice of gas, although deuterium gives larger Nernst velocities than hydrogen.  $\gamma_{\perp}^c$  is larger (factor of 10) for high- $Z$  material (see figure 8) and decreases with magnetisation; the more magnetised the plasma, the more hydrodynamic motion will play a role (until magnetic pressure becomes important).  $\Delta t / \tau_e$  is a measure of the experiment collisionality, i.e. how many electron-ion collisions a typical electron undergoes in the time since the laser was switched on  $\Delta t$ . Therefore, the more collisional (and as a consequence the more MHD-like) the experiment, the more hydrodynamic motion will also play a role in de-magnetising the laser-heated plasma.

Further variations in the experiment can be used to test theoretical predictions. Increasing the laser energy increases the temperature gradients, which is expected to increase the cavitation rate. Using a higher  $Z$  plasma can increase the Nernst coefficient. In the regime shown here, increasing the initial density increases the Nernst cavitation rate, primarily because the plasma magnetisation lowers.

The transition from MHD-like transport to kinetic-like transport could be probed by decreasing the laser spot size while keeping the intensity constant, thereby lowering the spatial scale relative to the mean-free path. The experiment times should be kept constant to maintain the same balance of Nernst to hydrodynamics (equation 9). While the cavitation rate will increase due to larger temperature gradients, the proton images only measure the path-integrated change in field strength. A proton image scaled in size with the laser radius is expected, with any differences due to non-local effects.

## B. Cross-Gradient-Nernst

The cross-gradient-Nernst is a magnetic transport velocity acting perpendicular to both the temperature gradient and the magnetic field (equation 21). Figure 8 demonstrates that the cross-gradient-Nernst velocity is large whenever the Nernst velocity is large. However, this does not necessarily mean that the cross-gradient-Nernst significantly alters the magnetic field profile. In the previous Nernst configuration, the cross-gradient-Nernst alters the field profile indistinguishably, as the plasma profile is effectively 1-D (not changing in  $\theta$  or along the field lines).

In this section the laser focus is changed such that the beam decreases with intensity along its path, giving a hotter plasma further along the cylindrical axis (high  $z$ ) and cooler plasma occupying a larger radius at low  $z$ . One standard deviation from the centre of the laser spot, the rays are at an angle of 3.6 degrees to the axis. The electron temperature profile at 0.5ns is shown in figure 4, with labels for the Nernst and cross-gradient-Nernst directions.

As before, the Nernst effect moves magnetic field radially outwards. The cross-gradient-Nernst, however, acts perpendicular to the 2-D simulation plane, moving the field azimuthally. The equation for the magnetic field advection velocity  $\underline{v}_{N\wedge}$  affects the magnetic field profile can be expanded from the form in equation 1 to:

$$\left[ \frac{\partial \underline{B}}{\partial t} \right]_{N\wedge} + (\underline{v}_{N\wedge} \cdot \nabla) \underline{B} = -\underline{B}(\nabla \cdot \underline{v}_{N\wedge}) + (\underline{B} \cdot \nabla) \underline{v}_{N\wedge} \quad (10)$$

The term on the left-hand side is now the convective derivative, i.e. how the magnetic field intensity changes moving with the flow. The first term on the right-hand side is then the field being compressed/rarefied by converging/diverging flows. Both the convective and compressive terms are zero for the cross-gradient-Nernst in these 2-D simulations, as both the field and velocities are uniform around  $\theta$ .

The final term in equation 10 represents the twisting of the magnetic field and is non-zero here. To demonstrate this, a magnetic field line is considered in isolation, passing between the heated (low  $z$  in figure 4) and unheated regions (large  $z$ ). At large  $z$ , the cross-gradient-Nernst velocity acting on this field line is zero, as there is no temperature gradient. At low  $z$ , cross-gradient-Nernst acts to advect the field line azimuthally. Between these two regions there is necessarily a twist in the field line, creating a  $\theta$  component. In reality the dependence of the cross-gradient-Nernst velocity on magnetisation in the twisted region results in both a field component into and out of the page at different regions.

Figure 4 shows the  $B_z$  and  $B_{\theta}$  magnetic field components at 0.5ns. The Nernst advection still occurs, lowering the axial field strength in the laser-heated region. A  $B_{\theta}$  field develops, up to a peak of 0.8T. While this is



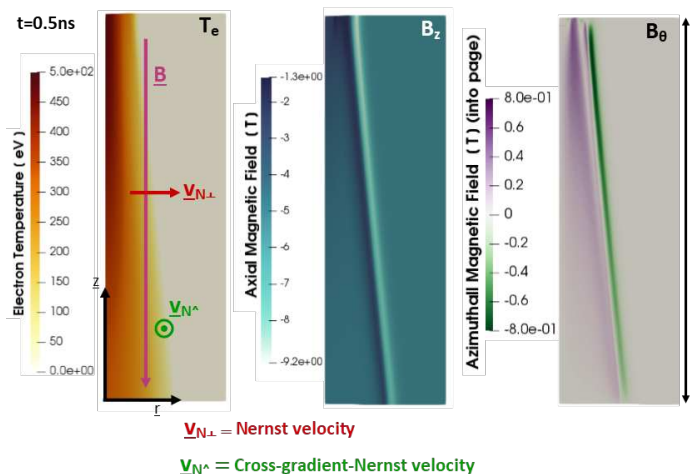


FIG. 4. Electron temperature and axial/azimuthal magnetic field components for the cross-gradient-Nernst configuration. Along the labelled magnetic field line the cross-gradient-Nernst moves out of the page at low  $Z$  and is zero at high  $Z$ , resulting in a twisted field component.

small compared to the 5T applied field, the twisting occurs in the same region depleted of axial field by regular Nernst advection, resulting in a peak twisting angle of 15 degrees.

The cross-gradient-Nernst velocity changes sign when the magnetic field is applied in the opposite direction, but the resulting  $B_\theta$  component is independent of the initial applied magnetic field.

While Nernst and cross-gradient-Nernst are significant in the same configuration, it is possible to measure  $B_\theta$  independently of the cavitating field by probing with protons along the laser axis. Figure 5 shows the synthetic proton radiograph with source situated at  $+z$ . The relative path-integrated strengths of the positive/negative  $B_\theta$  could be determined by looking at the outer/inner portions of the radiographs.

### C. Anisotropic Thermal Conduction

A configuration is now explored to assess the transition from unmagnetised thermal conduction to highly-magnetised conduction. The same conditions as the Nernst configuration are used (uniform under-dense laser-heated plasma with a background magnetic field), but with the magnetic field applied perpendicular to laser propagation. In Cartesian geometry, the laser is along  $-z$  and the magnetic field is in the  $x$  direction. The radial thermal conduction wave from the laser core is anisotropic, with thermal conduction in  $y$  suppressed due to magnetisation and heat-flow in  $x$  uninhibited.

Figure 6 shows 2-D  $x-y$  slices of the electron temperature profile at 0.5ns for various applied field strengths. The laser-heated region is hotter for the 5T case (340eV compared with 260eV for 1T), as thermal cooling along

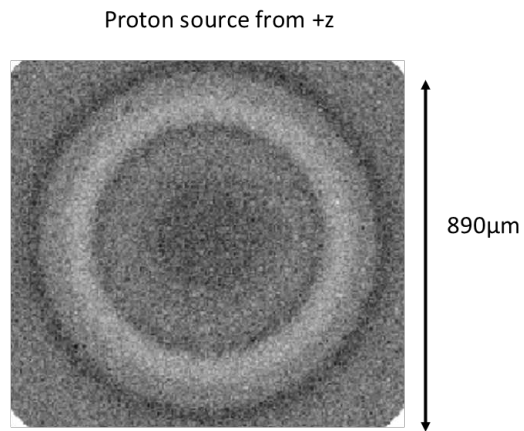


FIG. 5. Synthetic proton image at 0.5ns for the cross-gradient-Nernst configuration using a proton source at  $+z$ . The images have been re-scaled to the interaction region using the magnification.

$y$  is reduced. The peak magnetisation at this time is only  $\omega_e \tau_e \approx 1$  for the 1T case, corresponding to thermal conductivity suppression  $\kappa_\perp/\kappa_\parallel \approx 1/3$ . For the 5T case the peak magnetisation is  $\omega_e \tau_e > 10$ , with  $\kappa_\perp/\kappa_\parallel \approx 0.01$ . While magnetisation does not directly change the thermal conductivity along field lines ( $\kappa_\parallel$ ), the hotter core plasma results in greater heat-flows along  $x$  for higher magnetisations, increasing the heating radius. At 0.5ns the aspect ratio of the outer heat front is only 1.04 for 1T, increasing to 1.51 for 5T.

The anisotropic temperature profile can be diagnosed through self-emission (if the density remains relatively unperturbed) or by Thomson scattering. The relative extent of the heated region along  $y$  and  $x$  (along with a measurement of the peak temperature) will help constrain the analytic form for thermal conductivity magnetisation.

As with the Nernst configuration, a clear diagnostic signature here is aided by lack of hydrodynamic motion. A relation similar to 9 can be derived by comparing the hydrodynamic speed to the thermal conduction speed (rearranging perpendicular thermal conduction into the form  $\partial U_e/\partial t = \nabla \cdot (U_e \underline{v}_{\kappa\perp})$ , where  $\underline{v}_{\kappa\perp} = \kappa_\perp^c \tau_e \nabla T_e/m_e$ ):

$$\frac{|v_{Hydro}|}{|v_{\kappa\perp}|} = \frac{\Delta t Z m_e}{\tau_e m_i \kappa_\perp^c} \quad (11)$$

This is a variant on the Péclet number, relating advective and diffusive effects. It is no surprise that equations 9 and 11 give near-identical constraints on the experiment for hydrodynamics to be of secondary significance, as the thermal conduction and Nernst are inherently related. In fact, it is important to note that the Nernst effect will play a significant role in this configuration. If Nernst advection is larger than simulations anticipate, the plasma will become less magnetised, allowing larger perpendicular thermal conductivities. This could be er-

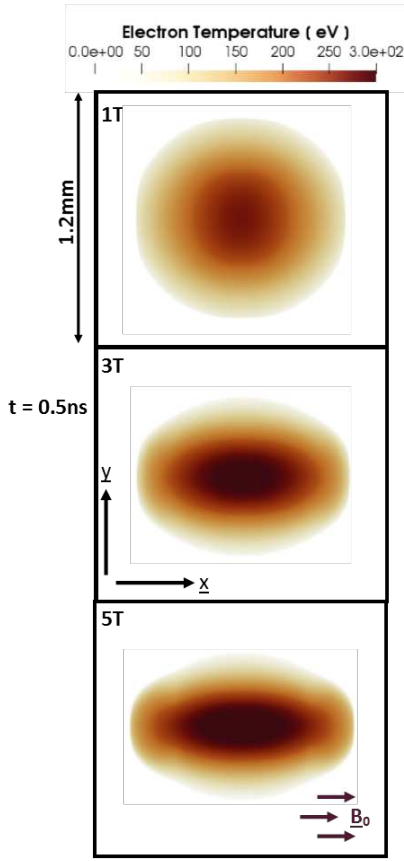


FIG. 6. Electron temperature profiles at 0.5ns with laser propagating into the page and a magnetic field applied along  $x$ . As the applied magnetic field is increased, the heat-flow anisotropy increases.

roniously interpreted as a different dependence of  $\kappa_{\perp}^c$  on  $\omega_e \tau_e$ . Therefore, further proton measurements in this configuration are valuable to avoid such misunderstandings. The Nernst configuration in section III A is preferred for diagnosing magnetic transport, as it avoids the complications of anisotropy by keeping the plasma uniform around the laser axis.

Kinetic effects will also play a role in this configuration. In the Nernst experiment heat-flow can be kept in the MHD regime through magnetisation (as measured under similar experimental conditions<sup>12</sup>). Here the heat-flow along the field lines will be dominated by electrons with a mean-free-path on the order of the temperature scale length, requiring kinetic modelling. For a more appropriate MHD comparison, the laser radius can be increased while keeping the intensity constant (to give the same  $\Delta t/\tau_e$  for equation 11).

#### D. Righi-Leduc

Righi-Leduc heat-flow is in the same direction as the cross-gradient-Nernst velocity; for an applied magnetic

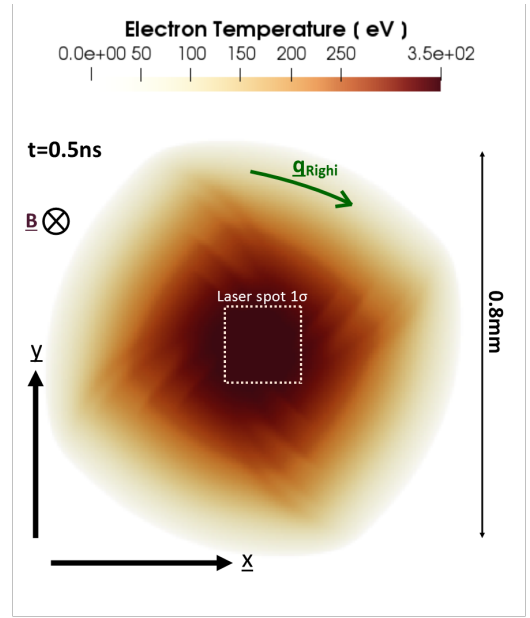


FIG. 7. Electron temperature profile in  $x - y$  with laser and magnetic field (3T) applied out of the plane. A square laser spot is used to enforce a temperature variation around  $\theta$ , which allows the Righi-Leduc heat-flow to modify the temperature distribution. The standard deviation of the square laser spot is shown with a dashed white line.

field in the same direction as the laser propagation, it acts around the azimuthal direction. In the cross-gradient-Nernst configuration (section III B) no azimuthal variations in plasma/magnetic field profile is required, as the magnetic field can twist. The heat-flow, however, only changes the electron temperature profile for variations in  $\theta$ . Therefore, a non-circular laser spot is required to bring about a clear diagnostic signature from Righi-Leduc. Here a square spot is considered.

Figure 7 shows a 2-D  $x - y$  slice of the electron temperature profile at 0.5ns with the laser and magnetic field propagating out of the page. The square laser spot edges are aligned with  $x$  and  $y$ , with ray powers set to a Gaussian of the maximum between  $x$  and  $y$ . The Righi-Leduc heat-flow rotates the electron energy profile. The rotated profile could be measured using self-emission or Thomson scattering. Reversal of the applied magnetic field direction swaps the rotation direction.

To further understand the rotation, an analytic form for the change in electron energy due to Righi-Leduc can be derived. Assuming magnetic field direction is constant (e.g.  $\hat{b} = (0, 0, 1)$  here) and with  $Z = \text{constant}$ , the rate of change of electron energy density is given by<sup>22</sup>:

$$\left[ \frac{\partial U_e}{\partial t} \right]_{\kappa_{\perp}} = \hat{b} \cdot [\nabla T_e \times \nabla \omega_e \tau_e] \frac{\partial \kappa_{\perp}^c}{\partial \omega_e \tau_e} \frac{n_e T_e \tau_e}{m_e} \quad (12)$$

For initially uniform density and field, frozen-in-flow gives  $|\mathbf{B}|/n_e = \text{constant}$ . Therefore, if the magnetic field is frozen into the flow (i.e. ignoring Nernst and cross-gradient-Nernst), this relation is zero (as



$\omega_e \tau_e \sim T^{3/2} |\underline{B}| / n_e$ ). In reality, the movement of magnetic field relative to the bulk plasma allows gradients in  $\omega_e \tau_e$ . These magnetisation gradients then reduce/enhance the Righi-Leduc heat-flow and result in accumulation/rarefaction of electron energy. The response of Righi-Leduc heat-flow to the magnetisation depends on the sign of  $\partial \kappa_\lambda^c / \partial \omega_e \tau_e$ , with  $\partial \kappa_\lambda^c / \partial \omega_e \tau_e > 0$  for  $\omega_e \tau_e \lesssim 0.1$  and  $\partial \kappa_\lambda^c / \partial \omega_e \tau_e < 0$  for  $\omega_e \tau_e \gtrsim 0.1$ . In the highly magnetised plasma simulated here, Righi-Leduc heat-flow reduces when it enters more magnetised regions.

Assuming uniform  $n_e$  (i.e. looking at time-scales over which the thermal evolution dominates over the hydrodynamic motion):

$$\left[ \frac{\partial U_e}{\partial t} \right]_{\kappa_\lambda} = \hat{b} \cdot [\nabla T_e \times \nabla |\underline{B}|] \frac{\partial \kappa_\lambda^c}{\partial \omega_e \tau_e} \frac{n_e T_e \tau_e^2 e}{m_e^2} \quad (13)$$

For a square laser pulse, the temperature initially peaks in  $\theta$  along  $y = x$  and  $y = -x$ . This results in Nernst demagnetisation of those regions, increasing the Righi-Leduc heat-flow. With the prevailing heat-flow travelling clockwise, the upstream heat-flow from the demagnetised region is increasing, while the downstream heat-flow is slowing down. This rotates the temperature profile clockwise, and the process continues.

The interplay between Righi-Leduc and Nernst have been studied theoretically and computationally for a similar regime<sup>23</sup>, although the cross-gradient-Nernst was not included. While figure 7 predominantly shows rotation of the temperature profile, higher applied magnetic field strengths result in instability growth, which is in agreement with conditions for the onset of the magnetothermal instability<sup>23</sup>.

#### IV. CONCLUSION

A magnetised under-dense platform has been outlined for the measurement of extended-MHD effects. The diverse operating range, low laser energies and relatively symmetric behaviour makes the base configuration suitable for measuring the Nernst velocity and its suppression at larger magnetisations for the first time. Magnetic field cavitation down the laser axis grows with time and can be diagnosed using proton deflectometry. In a regime where the Nernst velocity is much larger than the hydrodynamic motion, the proton measurement alone can be used to estimate the effect. Otherwise, a simultaneous measurement of plasma density and temperature can be used to give a Nernst estimate independent of simulations.

The laser spatial profile was then modified to show the effect of other extended-MHD terms. By allowing an angle between the heating beam and the applied magnetic field, the cross-gradient-Nernst can twist the field, allowing diagnosis independently of the regular Nernst by proton probing down the laser axis.

Anisotropic thermal conduction can then be demonstrated by using a magnetic field perpendicular to the heating beam, with heat flowing faster along the field lines. By modifying the applied field strength, the transition between unmagnetised and highly-magnetised regimes can be investigated.

Finally, Righi-Leduc heat-flow was shown to be important when using a square laser spatial profile, with azimuthal heat-flows rotating the electron energy profile. Applying the magnetic field in the opposite direction then reverses the rotation direction. This regime could also be used to observe the magnetothermal instability for the first time<sup>23</sup>.

Laser plasma instabilities could hinder the measurement of extended-MHD terms. The regime in this paper is estimated to be a factor of 20 above the ponderomotive filamentation threshold<sup>24</sup>. Filamentation could create locally hot regions where Nernst transport is high. The local spikes in temperature could slow the cavitation rate, as field can be trapped between two hot regions. The strong axial gradients will also increase the twisting of field by the cross-gradient-Nernst term. Ponderomotive filamentation could be mitigated by lowering the laser wavelength<sup>24</sup>, while changes to the laser intensity and resultant plasma temperature must ensure that Nernst transport still dominates over hydrodynamic expansion. Magnetisation of under-dense plasmas is also expected to increase thermal filamentation<sup>25</sup>, but in all regimes tried, the simulations remained unaffected.

By changing the laser spot radius and keeping the intensity constant, the experiment could be scaled into the non-local transport regime, increasing the relevance of the measurements to laser-plasma interaction regimes in ICF drive<sup>5,6,26</sup> and MagLIF pre-heat<sup>1</sup>. A further investigation of this transition will be the subject of a further publication comparing kinetic and MHD results.

The configuration outlined could also be modified to study the current-driven transport terms (equations 5 and 6). By comparing the Nernst velocity and Hall velocity (equation 7) it is clear that a larger magnetic field would be suitable, which both suppresses the Nernst and increases the electron current. While recent advances in magnetic field generation would allow for access to this regime<sup>27-29</sup>, an initially uniform magnetic field does not result in an electric current. Hydrodynamic motion is required to first perturb the magnetic field distribution, increasing the experiment complexity. While the laser drive will naturally change the field distribution to cause an electric current, the further perturbation of this field by the current-driven transport terms will have to be disentangled from the hydrodynamic motion by a comparison with the density profile.

## APPENDIX

### A. Magnetic Transport

The transport of magnetic flux in a plasma is typically written as an induction equation of the form<sup>14</sup>:

$$\begin{aligned} \frac{\partial \underline{B}}{\partial t} = & \nabla \times (\underline{v} \times \underline{B}) - \nabla \times \frac{\underline{j} \times \underline{B}}{n_e e} - \nabla \times \frac{\underline{\alpha} \cdot \underline{j}}{n_e^2 e^2} \\ & + \nabla \times \frac{\underline{\beta} \cdot \nabla T_e}{e} + \nabla \times \frac{\nabla P_e}{n_e e} \end{aligned} \quad (14)$$

Where the terms on the right-hand side represent bulk fluid advection, the Hall term, resistivity, thermally-driven transport and Biermann battery generation. The tensor transport coefficients  $\underline{\alpha}$  and  $\underline{\beta}$  are those defined by Epperlein and Haines<sup>30</sup>, with components parallel and perpendicular to the magnetic field.

While equation 14 fully describes the transport of magnetic fields in an extended-MHD plasma, the consequences of the equation are not immediately clear. Here the equation is re-written into a physically intuitive form, where each term acts to either advect, diffuse or generate magnetic field. This form is also simpler to implement into a code, with clearly defined stability criteria.

The thermally-driven magnetic transport term is expanded as:

$$\left[ \frac{\partial \underline{B}}{\partial t} \right]_{\underline{\beta}} = \nabla \times (\beta_{\parallel} \hat{\underline{b}} (\hat{\underline{b}} \cdot \nabla T_e) + \beta_{\perp} \hat{\underline{b}} \times (\nabla T_e \times \hat{\underline{b}}) + \beta_{\wedge} \hat{\underline{b}} \times \nabla T_e) \quad (15)$$

Where  $\hat{\underline{b}}$  is the magnetic field unit vector. This equation can be rearranged using the vector triple product  $[\hat{\underline{b}} (\hat{\underline{b}} \cdot \nabla T_e) = \nabla T_e - \hat{\underline{b}} \times (\nabla T_e \times \hat{\underline{b}})]$  and the fact that  $\nabla \times \beta_{\parallel} \nabla T_e$  is zero ( $\beta_{\parallel}$  is constant for a given ionisation) to give<sup>4</sup>:

$$\left[ \frac{\partial \underline{B}}{\partial t} \right]_{\underline{\beta}} = \nabla \times \left( -\frac{\beta_{\wedge}}{e |\underline{B}|} \nabla T_e \times \underline{B} - \frac{\beta_{\parallel} - \beta_{\perp}}{e |\underline{B}|} (\hat{\underline{b}} \times \nabla T_e) \times \underline{B} \right) \quad (16)$$

These terms are now in the common advection velocity form  $\nabla \times (\underline{v} \times \underline{B})$ . Therefore, the thermally-driven magnetic transport can be completely described as an advection of the magnetic field with velocity  $\underline{v}_N = \underline{v}_{N\perp} + \underline{v}_{N\wedge}$ . Using a tensor transport coefficient  $\underline{\gamma}$  further simplifies the equations, where:

$$\gamma_{\perp}^c = \frac{\beta_{\wedge}}{\omega_e \tau_e} \quad (17)$$

$$\gamma_{\wedge}^c = \frac{\beta_{\parallel} - \beta_{\perp}}{\omega_e \tau_e} \quad (18)$$

$$\underline{\gamma}^c = \underline{\gamma} \frac{m_e}{\tau_e} \quad (19)$$

The superscript <sup>c</sup> represents the dimensionless form of the coefficient, which is only dependent on the Hall parameter ( $\omega_e \tau_e$ ) and the plasma ionisation state  $Z$ . The magnetic field advection velocities are then:

$$\underline{v}_{N\perp} = -\frac{\beta_{\wedge}}{e |\underline{B}|} \nabla T_e = -\gamma_{\perp} \nabla T_e \quad (20)$$

which is called the Nernst velocity, and:

$$\underline{v}_{N\wedge} = -\frac{\beta_{\parallel} - \beta_{\perp}}{e |\underline{B}|} (\hat{\underline{b}} \times \nabla T_e) = -\gamma_{\wedge} (\hat{\underline{b}} \times \nabla T_e) \quad (21)$$

which is the cross-gradient-Nernst velocity<sup>4</sup>. The Nernst velocity can equally be written as  $\underline{v}_{N\perp} = -\gamma_{\perp} \hat{\underline{b}} \times (\nabla T_e \times \hat{\underline{b}})$  (i.e. removing the component parallel with the magnetic field). Note the change in subscripts from  $\underline{\beta}$  to  $\underline{\gamma}$ , which is to make clear that the Nernst velocity ( $\perp$ ) acts perpendicular to the magnetic field (in the  $\hat{\underline{b}} \times (\nabla T_e \times \hat{\underline{b}})$  direction), while the cross-gradient-Nernst ( $\wedge$ ) acts perpendicular to both the driving term (in this case  $\nabla T_e$ ) and the magnetic field. A clear benefit of re-writing the transport coefficients is the simple comparison of term magnitudes. As only the advection velocity component perpendicular to the magnetic field changes the field ( $[\frac{\partial \underline{B}}{\partial t}]_{\underline{v}_N} = \nabla \times (\underline{v}_N \times \underline{B}) = 0$  for  $\underline{v}_N$  parallel to  $\underline{B}$ ), both terms are only significant when the temperature gradient has a component perpendicular to the magnetic field. The ratio of the Nernst and cross-gradient-Nernst velocity magnitudes is simply:

$$\frac{|\underline{v}_{N\perp}|}{|\underline{v}_{N\wedge}|} = \frac{\gamma_{\perp}}{\gamma_{\wedge}} \quad (22)$$

Figure 8 plots the Nernst and cross-gradient-Nernst coefficients against magnetisation for  $Z = 1$  and  $\infty$ , showing that the cross-gradient-Nernst coefficient is similar in magnitude at low magnetisations ( $\approx 30\%$  lower for  $Z = 1$ ) and is larger at high magnetisations<sup>30</sup>. This suggests that in all cases where the Nernst velocity is large, the cross-gradient-Nernst velocity should also be evaluated. Another advantage of the  $\underline{\gamma}$  formulation is the simple monotonically-decreasing behaviour of the two coefficients with magnetisation.

The resistive magnetic transport term in equation 14 is typically expanded as:

$$\left[ \frac{\partial \underline{B}}{\partial t} \right]_{\underline{\alpha}} = -\nabla \times \left( \frac{\alpha_{\parallel}}{e^2 n_e^2} \hat{\underline{b}} (\hat{\underline{b}} \cdot \underline{j}) + \frac{\alpha_{\perp}}{e^2 n_e^2} \hat{\underline{b}} \times (\underline{j} \times \hat{\underline{b}}) - \frac{\alpha_{\wedge}}{e^2 n_e^2} \hat{\underline{b}} \times \underline{j} \right) \quad (23)$$

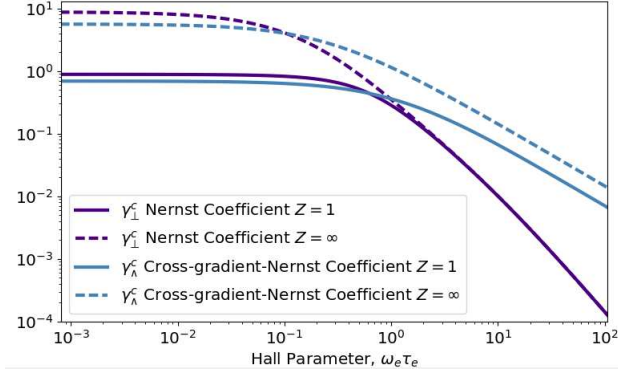


FIG. 8. The dependence of the  $\underline{\gamma}$  magnetic transport coefficients on  $\omega_e \tau_e$  for  $Z = 1$  (solid line) and  $Z = \infty$  (dashed).  $\gamma_\lambda$ , the cross-gradient-Nernst transport coefficient, is approximately equal to or larger than the regular Nernst coefficient,  $\gamma_\perp$  for all magnetisations. Data from<sup>30</sup>.

Using the same methodology as for the thermally-driven terms, this can be re-arranged into the form of magnetic field advection velocities. In this case, however, the parallel term contains an additional resistive component, as  $\nabla \times (\alpha_\parallel / \mu_0 e^2 n_e^2) \underline{j} \neq 0$ :

$$\left[ \frac{\partial \underline{B}}{\partial t} \right]_{\underline{\alpha}} = -\nabla \times \left( \frac{\alpha_\parallel}{\mu_0 e^2 n_e^2} \nabla \times \underline{B} \right) + \nabla \times \left( \left( \frac{\alpha_\perp - \alpha_\parallel}{e^2 n_e^2 |\underline{B}|} \underline{j} \times \hat{b} - \frac{\alpha_\lambda}{e^2 n_e^2 |\underline{B}|} \underline{j} \right) \times \underline{B} \right) \quad (24)$$

where the first term on the right is diffusive. The latter two terms become collisional current-driven transport velocities  $\underline{v}_{jB} = \underline{v}_{jB\perp} + \underline{v}_{jB\lambda}$ . A new tensor transport coefficient  $\underline{\delta}$  is also used here to simplify the equations:

$$\delta_\perp^c = \frac{\alpha_\perp^c}{\omega_e \tau_e} \quad (25)$$

$$\delta_\lambda^c = \frac{\alpha_\perp^c - \alpha_\parallel^c}{\omega_e \tau_e} \quad (26)$$

$$\underline{\delta} = \underline{\delta}^c \frac{1}{en_e} \quad (27)$$

The magnetic field advection velocities are then:

$$\underline{v}_{jB\perp} = -\frac{\alpha_\perp}{e^2 n_e^2 |\underline{B}|} \underline{j} = -\delta_\perp \underline{j} \quad (28)$$

$$\underline{v}_{jB\lambda} = \frac{\alpha_\perp - \alpha_\parallel}{e^2 n_e^2 |\underline{B}|} \underline{j} \times \hat{b} = \delta_\lambda \underline{j} \times \hat{b} \quad (29)$$

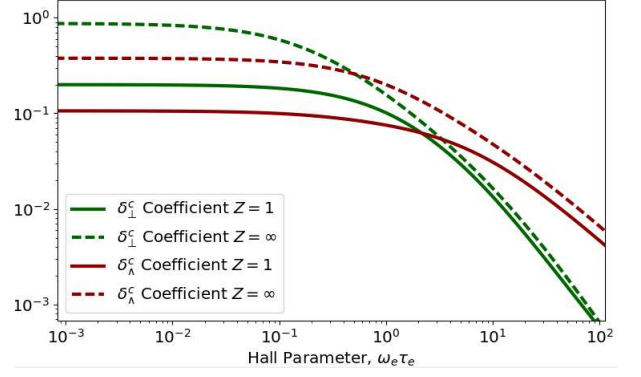


FIG. 9. The dependence of the  $\underline{\delta}$  magnetic transport coefficients on  $\omega_e \tau_e$  for  $Z = 1$  (solid line) and  $Z = \infty$  (dashed). Note the similarity with the  $\gamma^c$  coefficients in figure 8. Data from<sup>30</sup>.

The collisionless Hall term from equation 14 can also be manipulated into a velocity:

$$\underline{v}_{Hall} = -\frac{\underline{j}}{en_e} \quad (30)$$

i.e. the magnetic field moves with the bulk electron motion rather than the ion population. The resistive advection velocities from equations 28 and 29 are clearly related to the Hall term, and will be referred to as the collisional corrections to the Hall term. Figure 9 compares the magnitude of  $\delta_\perp^c$  and  $\delta_\lambda^c$  for  $Z = 1$  and  $\infty$ , with both monotonically decreasing for increasing magnetisation.

Overall, the magnetic transport equation can be re-written as in equation 2.

In this rewritten form, each term is simple to implement in an MHD code, where advection and diffusion operations are commonplace. The stability limits are also clear, with the CFL condition for the advection in 1-D<sup>31</sup>:

$$\Delta t_{advection} \leq \frac{\Delta x}{|\underline{v}_B|} \quad (31)$$

and the Von Neumann stability limit for the diffusion:

$$\Delta t_{diffusion} \leq \frac{\Delta x^2 \mu_0 e^2 n_e^2}{2\alpha_\parallel} \quad (32)$$

It is interesting to note that the remaining transport coefficients in the re-written induction equation have a simple dependence: increasing with  $Z$ , maximum at zero magnetisation and monotonically decreasing for increasing  $\omega_e \tau_e$  (apart from the  $\alpha_\parallel$  term, which is constant).

## B. Thermal Transport

The electron heat-flow equation is<sup>14</sup>:

$$\left[ \frac{\partial U_e}{\partial t} \right]_{\underline{q}} = -\nabla \cdot \underline{q}_e = -\nabla \cdot \left( -\underline{\kappa} \cdot \nabla T_e - \frac{U_e}{en_e} \beta \cdot \underline{j} - \frac{U_e}{en_e} \underline{j} \right) \quad (33)$$

The first term on the right-hand side represents thermal conduction, then electro-thermal terms and finally the heat-flow associated with the flow of charge. The thermal diffusion component can be expanded as:

$$\underline{q}_\kappa = -\kappa_{\parallel} \hat{\underline{b}} (\hat{\underline{b}} \cdot \nabla T_e) - \kappa_{\perp} \hat{\underline{b}} \times (\nabla T_e \times \hat{\underline{b}}) - \kappa_{\wedge} \hat{\underline{b}} \times \nabla T_e \quad (34)$$

The first term represents the heat-flow along magnetic field lines, which remains unchanged by magnetisation. The second term is the heat-flow perpendicular to the field and decreases monotonically with magnetisation. The final term is the Righi-Leduc heat-flow, which represents heat-flow deflected by the magnetic field into the direction perpendicular to both the magnetic field and the temperature gradient.

By using simplified operators the connection between thermally-driven electron energy transport and magnetic transport can be made clear. Here  $\nabla_{\parallel} T_e = \hat{\underline{b}} (\hat{\underline{b}} \cdot \nabla T_e)$  and  $\nabla_{\perp} T_e = \hat{\underline{b}} \times (\nabla T_e \times \hat{\underline{b}})$  are used. The magnetic field advection velocity due to temperature gradients can be re-written alongside the flow of electron energy due to temperature gradients, as in equations 3 and 4.

The current-driven heat-flows are best understood by using the velocity of the electron population relative to the ions,  $-\underline{j}/en_e$ . The change in electron energy due to the current (last two terms in equation 33) can then be written:

$$\left[ \frac{\partial U_e}{\partial t} \right]_{\underline{j}} + \underline{v}_j \cdot \nabla U_e = -U_e \nabla \cdot \underline{v}_j \quad (35)$$

$$\underline{v}_j = -\frac{\underline{j}}{en_e} - \beta_{\parallel} \hat{\underline{b}} (\hat{\underline{b}} \cdot \frac{\underline{j}}{en_e}) - \beta_{\perp} \hat{\underline{b}} \times (\frac{\underline{j}}{en_e} \times \hat{\underline{b}}) - \beta_{\wedge} \hat{\underline{b}} \times \frac{\underline{j}}{en_e} \quad (36)$$

i.e. the electron energy moves with the electron population relative to the ions, with collisional corrections. The comparison with the magnetic transport becomes even more clear by using  $\underline{j}_{\parallel} = \hat{\underline{b}} \cdot (\hat{\underline{b}} \cdot \underline{j})$  and  $\underline{j}_{\perp} = \hat{\underline{b}} \times (\underline{j} \times \hat{\underline{b}})$ . The current-driven velocities transporting the magnetic field and electron energies are then written as in equations 5 and 6.

## ACKNOWLEDGEMENTS

The results reported in this paper were obtained using the Imperial College High Performance Computer Cx1. This work was supported by NNSA under DOE Cooperative Agreement DE-NA0003764 and has been carried out within the framework of the EUROfusion Consortium

as well as receiving funding from the Euratom research and training programme 2014-2018 under grant agreement No. 633053 (project reference CfP-AWP17-IFE-CCFE-01). The views and opinions expressed herein do not necessarily reflect those of the European Commission.

## REFERENCES

- <sup>1</sup>R. D. McBride and S. A. Slutz, ‘‘A semi-analytic model of magnetized liner inertial fusion,’’ *Physics of Plasmas* **22**, 052708 (2015).
- <sup>2</sup>L. J. Perkins, D. D.-M. Ho, B. G. Logan, G. B. Zimmerman, M. A. Rhodes, D. J. Strozzi, D. T. Blackfield, and S. A. Hawkins, ‘‘The potential of imposed magnetic fields for enhancing ignition probability and fusion energy yield in indirect-drive inertial confinement fusion,’’ *Physics of Plasmas* **24**, 062708 (2017).
- <sup>3</sup>C. A. Walsh, K. McGlinchey, J. K. Tong, B. D. Appelbe, A. Crilly, M. Zhang, and J. P. Chittenden, ‘‘Perturbation Modifications by Pre-magnetisation in Inertial Confinement Fusion Implosions,’’ *Physics of Plasmas* **096**, 1–12 (2018).
- <sup>4</sup>J. R. Davies, R. Betti, P.-Y. Chang, and G. Fiksel, ‘‘The importance of electrothermal terms in Ohm’s law for magnetized spherical implosions,’’ *Physics of Plasmas* **22** (2015), 10.1063/1.4935286.
- <sup>5</sup>W. A. Farmer, J. M. Koning, D. J. Strozzi, D. E. Hinkel, L. F. Berzak Hopkins, O. S. Jones, and M. D. Rosen, ‘‘Simulation of self-generated magnetic fields in an inertial fusion hohlraum environment,’’ *Physics of Plasmas* **24**, 052703 (2017).
- <sup>6</sup>D. W. Hill and R. J. Kingham, ‘‘Enhancement of Pressure Perturbations in Ablation due to Kinetic Magnetised Transport Effects under Direct-Drive ICF relevant conditions,’’ *Arxiv* (2017), arXiv:1712.02663.
- <sup>7</sup>C. Walsh, J. Chittenden, K. McGlinchey, N. Niasse, and B. Appelbe, ‘‘Self-Generated Magnetic Fields in the Stagnation Phase of Indirect-Drive Implosions on the National Ignition Facility,’’ *Physical Review Letters* **118**, 155001 (2017).
- <sup>8</sup>L. Gao, P. Nilson, I. Igumenshchev, M. Haines, D. Froula, R. Betti, and D. Meyerhofer, ‘‘Precision Mapping of Laser-Driven Magnetic Fields and Their Evolution in High-Energy-Density Plasmas,’’ *Physical Review Letters* **114**, 215003 (2015).
- <sup>9</sup>C. K. Li, F. H. Séguin, J. A. Frenje, J. R. Rygg, R. D. Petrasso, R. P. J. Town, P. A. Amendt, S. P. Hatchett, O. L. Landen, A. J. Mackinnon, P. K. Patel, V. A. Smalyuk, T. C. Sangster, and J. P. Knauer, ‘‘Measuring E and B Fields in Laser-Produced Plasmas with Monoenergetic Proton Radiography,’’ *Physical Review Letters* **97** (2006), 10.1103/PhysRevLett.97.135003.
- <sup>10</sup>P. M. Nilson, L. Willingale, M. C. Kaluza, C. Kamperidis, S. Minardi, M. S. Wei, P. Fernandes, M. Notley, S. Bandyopadhyay, M. Sherlock, R. J. Kingham, M. Tatarakis, Z. Najmudin, W. Rozmus, R. G. Evans, M. G. Haines, A. E. Dangor, and K. Krushelnick, ‘‘Magnetic Reconnection and Plasma Dynamics in Two-Beam Laser-Solid Interactions,’’ *Physical Review Letters* **97**, 255001 (2006).
- <sup>11</sup>M. J.-E. Manuel, C. K. Li, F. H. Séguin, J. Frenje, D. T. Casey, R. D. Petrasso, S. X. Hu, R. Betti, J. D. Hager, D. D. Meyerhofer, and V. A. Smalyuk, ‘‘First measurements of Rayleigh-Taylor-induced magnetic fields in laser-produced plasmas.’’ *Physical review letters* **108**, 255006 (2012).
- <sup>12</sup>D. H. Froula, J. S. Ross, B. B. Pollock, P. Davis, A. N. James, L. Divol, M. J. Edwards, A. A. Offenberger, D. Price, R. P. J. Town, G. R. Tynan, and S. H. Glenzer, ‘‘Quenching of the Nonlocal Electron Heat Transport by Large External Magnetic Fields in a Laser-Produced Plasma Measured with Imaging Thomson Scattering,’’ *Physical Review Letters* **98** (2007), 10.1103/PhysRevLett.98.135001.
- <sup>13</sup>C. P. Ridgers, R. J. Kingham, and A. G. R. Thomas, ‘‘Magnetic Cavitation and the Reemergence of Nonlocal Transport in Laser

- Plasmas,” *Physical Review Letters* **100** (2008), 10.1103/PhysRevLett.100.075003.
- <sup>14</sup>S. I. Braginskii, “Transport Processes in a Plasma,” in *Reviews of Plasma Physics*, Vol. 1 (1965) p. 205.
- <sup>15</sup>A. Ciardi, S. V. Lebedev, A. Frank, E. G. Blackman, J. P. Chittenden, C. J. Jennings, D. J. Ampleford, S. N. Bland, S. C. Bott, J. Rapley, G. N. Hall, F. A. Suzuki-Vidal, A. Marocchino, T. Lery, and C. Stehle, “The evolution of magnetic tower jets in the laboratory,” in *Physics of Plasmas*, Vol. 14 (2007) arXiv:0611441 [astro-ph].
- <sup>16</sup>P. Sharma and G. W. Hammett, “Preserving monotonicity in anisotropic diffusion,” *Journal of Computational Physics* **227** (2007), 10.1016/j.jcp.2007.07.026, arXiv:0707.2616.
- <sup>17</sup>J. P. Knauer, O. V. Gotchev, P. Y. Chang, D. D. Meyerhofer, O. Polomarov, R. Betti, J. a. Frenje, C. K. Li, M. J.-E. Manuel, R. D. Petrasso, J. R. Rygg, and F. H. Séguin, “Compressing magnetic fields with high-energy lasers,” *Physics of Plasmas* **17** (2010), 10.1063/1.3416557.
- <sup>18</sup>L. Willingale, S. P. D. Mangles, P. M. Nilson, R. J. Clarke, A. E. Dangor, M. C. Kaluza, S. Karsch, K. L. Lancaster, W. B. Mori, Z. Najmudin, J. Schreiber, A. G. R. Thomas, M. S. Wei, and K. Krushelnick, “Collimated Multi-MeV Ion Beams from High-Intensity Laser Interactions with Underdense Plasma,” *Physical Review Letters* **96**, 245002 (2006).
- <sup>19</sup>L. Willingale, A. G. R. Thomas, P. M. Nilson, M. C. Kaluza, S. Bandyopadhyay, A. E. Dangor, R. G. Evans, P. Fernandes, M. G. Haines, C. Kamperidis, R. J. Kingham, S. Minardi, M. Notley, C. P. Ridgers, W. Rozmus, M. Sherlock, M. Tatarakis, M. S. Wei, Z. Najmudin, and K. Krushelnick, “Fast Advection of Magnetic Fields by Hot Electrons,” *Physical Review Letters* **105** (2010), 10.1103/PhysRevLett.105.095001.
- <sup>20</sup>A. J. Mackinnon, P. K. Patel, R. P. Town, M. J. Edwards, T. Phillips, S. C. Lerner, D. W. Price, D. Hicks, M. H. Key, S. Hatchett, S. C. Wilks, M. Borghesi, L. Romagnani, S. Kar, T. Toncian, G. Pretzler, O. Willi, M. Koenig, E. Martinolli, S. Lepape, A. Benuzzi-Mounaix, P. Audebert, J. C. Gauthier, J. King, R. Snavely, R. R. Freeman, and T. Boehlly, “Proton radiography as an electromagnetic field and density perturbation diagnostic,” *Review of Scientific Instruments* **75** (10 11) (2004), 10.1063/1.1788893.
- <sup>21</sup>J. P. Brodrick, M. Sherlock, W. A. Farmer, A. S. Joglekar, R. Barrois, J. Wengraf, J. J. Bissell, R. J. Kingham, D. Del Sorbo, M. P. Read, and C. P. Ridgers, “Incorporating Kinetic Effects on Nernst Advection in Inertial Fusion Simulations,” *Arxiv* (2018), arXiv:1803.05801.
- <sup>22</sup>J. Bissell, *Magnetised transport and instability in laser produced plasmas*, Ph.D. thesis, Imperial College London (2012).
- <sup>23</sup>J. J. Bissell, C. P. Ridgers, and R. J. Kingham, “Field Compressing Magnetothermal Instability in Laser Plasmas,” *Physical Review Letters* **105** (2010), 10.1103/PhysRevLett.105.175001.
- <sup>24</sup>D. H. Froula, L. Divol, N. B. Meezan, S. Dixit, J. D. Moody, P. Neumayer, B. B. Pollock, J. S. Ross, and S. H. Glenzer, “Ideal laser-beam propagation through high-temperature ignition Hohlraum plasmas,” *Physical Review Letters* **98** (2007), 10.1103/PhysRevLett.98.085001.
- <sup>25</sup>H. C. Watkins and R. J. Kingham, “Magnetised thermal self-focusing and filamentation of long-pulse lasers in plasmas relevant to magnetised ICF experiments,” *Phys. Plasmas* **25**, 92701 (2018).
- <sup>26</sup>I. V. Igumenshchev, A. B. Zylstra, C. K. Li, P. M. Nilson, V. N. Goncharov, and R. D. Petrasso, “Self-generated magnetic fields in direct-drive implosion experiments,” *Physics of Plasmas* **21** (2014), 10.1063/1.4883226.
- <sup>27</sup>J. J. Santos, M. Bailly-Grandvaux, L. Giuffrida, P. Forestier-Colleoni, S. Fujioka, Z. Zhang, P. Korneev, R. Bouillaud, S. Dorard, D. Batani, M. Chevrot, J. E. Cross, R. Crowston, J.-L. Dubois, J. Gazave, G. Gregori, E. D’Humières, S. Hulin, K. Ishihara, S. Kojima, E. Loyez, J.-R. Marquès, A. Morace, P. Nicolai, O. Peyrusse, A. Poyé, D. Raffestin, J. Ribolzi, M. Roth, G. Schaumann, F. Serres, V. T. Tikhonchuk, P. Vacar, and N. Woolsey, “Laser-driven platform for generation and characterization of strong quasi-static magnetic fields,” *New Journal of Physics* **17**, 083051 (2015).
- <sup>28</sup>K. F. F. Law, M. Bailly-Grandvaux, A. Morace, S. Sakata, K. Matsuo, S. Kojima, S. Lee, X. Vaisseau, Y. Arikawa, A. Yogo, K. Kondo, Z. Zhang, C. Bellei, J. J. Santos, S. Fujioka, and H. Azechi, “Direct measurement of kilo-tesla level magnetic field generated with laser-driven capacitor-coil target by proton deflectometry,” *Applied Physics Letters* **108**, 091104 (2016).
- <sup>29</sup>S. Fujioka, Z. Zhang, K. Ishihara, K. Shigemori, Y. Hironaka, T. Johzaki, A. Sunahara, N. Yamamoto, H. Nakashima, T. Watanabe, H. Shiraga, H. Nishimura, and H. Azechi, “Kilo-tesla Magnetic Field due to a Capacitor-Coil Target Driven by High Power Laser,” *Scientific Reports* **3**, 1170 (2013).
- <sup>30</sup>E. M. Epperlein and M. G. Haines, “Plasma transport coefficients in a magnetic field by direct numerical solution of the Fokker-Planck equation,” *Physics of Fluids* **29** (1986), 10.1063/1.865901.
- <sup>31</sup>R. Courant, K. Friedrichs, and H. Lewy, “On the Partial Difference Equations of Mathematical Physics,” *IBM Journal of Research and Development* **11**, 215–234 (1967).